Sensors and Actuators A 162 (2010) 61–71

Contents lists available at ScienceDirect

Sensors and Actuators A: Physical

journal homepage: www.elsevier.com/locate/sna

Solid–gas surface effect on the performance of a MEMS-class nozzle for micropropulsion

José Antonio Moríñigo [a,*], José Hermida-Quesada [b,1]

[a] Dpto. Programas Espaciales, Instituto Nacional de Técnica Aeroespacial, Ctra. Ajalvir km. 4, Torrejón de Ardoz, 28850 Madrid, Spain
[b] Dpto. de Aerodinámica y Propulsión, Instituto Nacional de Técnica Aeroespacial, Ctra. Ajalvir km. 4, Torrejón de Ardoz, 28850 Madrid, Spain

ARTICLE INFO

Article history:
Received 14 December 2009
Received in revised form 28 April 2010
Accepted 8 June 2010
Available online 17 June 2010

Keywords:
Coupled solid–fluid simulation
Micronozzle
Micropropulsion
Slip-flow

ABSTRACT

Steady-state performance of a three-dimensional flat-shaped micronozzle in underexpanded cold- and hot-gas operation has been analysed with numerical simulation. The flow regime is supersonic and characterized by a Knudsen number varying from slightly slip-flow by the nozzle throat, to moderate transitional regime near the nozzle lip. A second-order in Knudsen model has been implemented to incorporate the effects of the slip in velocity and temperature jump into a Navier–Stokes finite-volume commercial code, so fully thermal coupling between the gas and solid portions of the computational domain is imposed and the heat balance at the solid surface is enforced from the temperature jump at the interface. The results stress the strong dependence between solid–gas surface temperature and gas expansion across the nozzle, favoured by the high-speed of the flow that enhances the heat-transfer by the solid surface. The results also show that thermal coupling at the solid–gas surface becomes an essential part of the modelling for reliable prediction of the nozzle wall temperature and therefore of the performance delivered. As viscous dissipation leads to a performance drop that may be serious in too lengthy nozzles, the maximization of performance demands to consider the three-dimensional nature of the high-speed flow in simulations with microgeometries.

1. Introduction

The conception and engineering of very small spacecrafts (S/Cs) with stringent in-orbit requirements passes through incorporating the propulsion technology onboard, in a scale compatible with the constrains stated by the space mission and vehicle and so providing the performances required by the orbital manoeuvres and attitude control of the spacecraft during the mission lifetime. But not only small S/Cs demand the development of advanced microthrusters, it is also a challenge in those satellites of more conventional size that require attitude control of unprecedented accuracy to compensate the effects of the space media on the S/Cs location (that is, drag, solar radiation pressure or celestial bodies attraction, to cite some). Hence, micropropulsion arises as an enabling technology in both applications, with special relevance within the recent years since several dedicated small launchers are under development to serve nano- and pico-satellites to more precise orbits, so the accurate orbit control is foreseen essential in the next-generation missions that demand tiny impulse bits (i.e., the minimum amount of impulse that can be delivered each time a thruster is fired) and thrust levels within the range of micro- to a few milli-Newton. One example of these missions is the so-called flying formation, where a group of small S/Cs maintains its relative locations by means of frequent thrusters firings.

A variety of concepts have remained under discussion in the chemical micropropulsion area during the last two decades and a first rough classification of microthrusters can be provided attending to the temperature of the gas generated or supplied. Then, it follows the distinction between those devices where the expansion of a cold gas takes place; and those relying on the catalytic decomposition or volumetric combustion into a microtank, that raises the temperature prior to the expansion through a miniaturized nozzle. The manufacturing complexity, integration issues or performance delivered constitute aspects that change significantly depending on the device configuration and physical processes involved, many of which still remains under preliminary investigation or in an early stage of their ground tests performance characterization. Besides, space missions impose a series of specific constrains, like for the mass or power demand, that can be only fulfilled by a subclass of propulsive concepts. In this sense, the criteria of simplicity, versatility and ease of manufacturing have driven the research in chemical micropropulsion to weight up some of the concepts above oth-

* Corresponding author. Tel.: +34 91 520 1351; fax: +34 91 520 1384.
E-mail addresses: morignigoja@inta.es (J.A. Moríñigo), hermidaj@inta.es (J. Hermida-Quesada).
[1] Tel.: +34 91 5201457.

0924-4247/$ – see front matter © 2010 Elsevier B.V. All rights reserved.
doi:10.1016/j.sna.2010.06.006

ers, as it is the case of the arrayed MEMS-class microthrusters based on solids decomposition (also termed gas generators or solid-propellant MEMS), which are at the beginning of their in-orbit demonstration. A review of the diverse microthruster options may be found in [1]. The present study addresses the expansion of molecular nitrogen (N_2) through a MEMS-class nozzle as it is the predominant component in many propellant decompositions occurring in chemical microthrusters (that corresponds to the so-called HOT-flow conditions), as well as in blow-down operated thrusters with the gas stored at ambient conditions into a pressurized tank (termed COLD-flow conditions). Basically the gas enters a microchamber or it is generated by a combustion process inside it, then it expands through a convergent–divergent nozzle and finally outflows to the space of very low pressure (near vacuum media). In this process, the combined effect of the small geometrical scale of the device and the low pressure level of the ambient is responsible of the progressive rarefaction of the gas, that must be considered in the modelling. In addition, the large surface area-to-volume ratio characteristic of MEMS and the high thermal conductivity of the solid portion of the nozzle component makes the heat exchange at the inner wall of the nozzle a key aspect, as it drives the performance to a large extent. Hence, modelling the thermal balance at the solid–gas surface turns to be essential for reliable predictions of performance. It will be shown that, in cold flow expansions, the nozzle material block will tend to deliver a net heat flux to the gas as it flows through the nozzle, acting then as a heat source; on the contrary, in hot flow expansions, the material acts as a heat sink and the expanding gas releases some of its heat to the surrounding material, heating it up. Albeit several investigations of micronozzle high-speed flows have been accomplished with Navier–Stokes (NS) and Direct Simulation Monte Carlo (DSMC), to the authorsĭ knowledge only a few three-dimensional (3D) simulations of high-speed gas flow with enforced thermal coupling between gas and the solid side of the microsystem have been reported [2–7] (the solid–gas surface temperature is not imposed prior to starting the simulation, but it results from the simulation). The present investigation focuses on this gas regime using a model that incorporates the solid–gas full-coupling and slip-flow at the surface, extending to 3D geometries the previous work conducted by the authors with axisymmetrical modelling in [7,8]. A robust second-order in Knudsen number (Kn) implementation of the slip velocity and temperature jump conditions is presented and applied to the computation of solid–gas coupled supersonic flow in a MEMS-class nozzle intended for micropropulsion. The applicability of second-order boundary conditions to steady and transient gasflow of higher Knudsen number under a continuous approach has been demonstrated by other authors in microchannels configurations against experimental data [9,10] and DSMC [11] and the practical extension of the slip-flow regime with marginal validity up to about $Kn = 0.3$–0.4 has been suggested.

The paper is organised as follows. Section 2 discusses the rarefaction of the expanding gas and the validity of the adopted continuous approach based on the Navier–Stokes equations. Then, the boundary conditions and coupling algorithm at the solid–gas surface are presented in Section 3 with the overall description of the numerical approach. In Section 4 a comparison of the prediction against DSMC for varying momentum accommodation coefficient is provided for a 3D flat-shaped micronozzle geometry. Compressibility and rarefaction effects are taken into account into the modelling (no attempt of analysing the effect of the solid–gas surface roughness is done, its effect is linked to the accommodation coefficients). Following the validation of the methodology, the discussion of the performance achieved by the micronozzle at operating conditions corresponding to cold and hot flow follows. Finally, some conclusions are given.

2. Flow regimes and their simulation

The small Reynolds number (Re) of the flow through micronozzles results of their small dimension and moderate-to-low operating pressures at the gas supply or combustion chamber, with typical values below Re = 1000 in cold-gas systems and even lower in hot-gas-based MEMS (of characteristic size around 100 μm). An immediate consequence of this low Reynolds number is the intense viscous dissipation that arises, which is responsible of the significant viscous losses occurring downstream the nozzle throat due to the friction mechanism. The increase of temperature and deceleration in Mach number (M) of the bulk flow due to the conversion of kinetic energy into heat, modifies the heat-flux balance near the nozzle wall. The relationship among the effects of viscosity (Reynolds number), compressibility (Mach number) and rarefaction (Knudsen number) is implicit in the following expression

$$Re = \sqrt{\frac{\gamma\pi}{2}}\frac{M}{Kn} \tag{1}$$

However and in clear contrast with other kind of microflows, high-speed viscous flow exhibits a large variation of fluid properties stream- and crosswise, that makes inappropriate to provide a global Knudsen number definition to characterize the flow within. In micronozzles, gasflow may evolve from incipient rarefaction near the throat to moderate- or even high-rarefied regime near the lip and outside the nozzle, where the gas suffers a strong expansion. Hence, it seems meaningless to build a global Knudsen number $Kn = \lambda/l$ (ratio of the molecular mean free path of the molecules λ to the characteristic lengthscale l of the flow) based on averaging the gas properties across the fluid domain and using an overall dimension of the flow. Thus, a more rigorous procedure is to define a local Kn at each flow zone. One interesting way to account for these large variations of Kn is to use an intrinsic lengthscale derived from the gas thermodynamic and kinematic quantities and their associated macroscopic gradients, then to evaluate the Knudsen number according to it.

Attending to the Knudsen number, a classification of the degree of rarefaction can be accomplished into four regimes, as follows:

- $Kn < 0.01$: the gas is considered to be a continuum. In strict sense, continuum regime ranges up to $Kn \sim 10^{-3}$, but in practical calculations this limit is usually relaxed and shifted to the above-mentioned value of about $Kn \sim 0.01$. In this regime, collisions of molecules with the wall are transmitted almost instantaneously to the rest of the flow, then the NS equations with no-slip boundary conditions behave accurate to describe the bulk flow and plausible discrepancies of predictions are associated to other causes than rarefaction effects.
- $0.01 < Kn < 0.1$: slip-flow regime. The mean free path is small in comparison with the characteristic dimension of the microdevice, but it cannot be disregarded. The local non-equilibrium effects can be considered confined adjacent to the wall (into the so-called Knudsen layer of about one to two times the mean free path). From the modelling standpoint, the rarefaction effects occurring in the wall vicinity can be efficiently captured under the NS-based approach supplementing the equations with slip-flow boundary conditions to consider the apparent velocity slip and temperature jump at the wall in the macroscopic scale. The upper bound of this regime, typically prescribed of about $Kn = 0.1$–0.15, sets the limit of validity of the assumption of local rarefaction effects inserted in the continuum formulation as a correction at the wall. Consequently, higher Kn implies thicker Knudsen layers and more pronounced rarefaction effects, thus the implementation of a higher-order slip-flow relations seems to be advantageous to extend the range of validity of the NS description of steady and time-dependent flows beyond $Kn = 0.1$, therefore the interest in

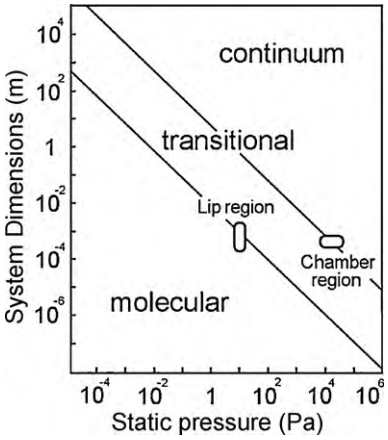

Fig. 1. Map of gas regimes and location of the flow rarefaction conditions in the micronozzle chamber and lip zone for validation and operating supply pressure (local lengthscale and standard temperature is used for plotting).

Table 1
3D-Flat micronozzle geometry.

Divergent half-angle	α_{div}	15°
Convergent half-angle	α_{con}	22°
Divergent length	L_{div}	5038 μm
Throat height	h_{th}	300 μm
Expansion area ratio	A_e/A_{th}	10
Inlet to throat area ratio	A_{in}/A_{th}	2.2

these type of formulations supplementing the NS equations is clear.

- $0.1 < Kn < 10$: transition (or intermediate) regime. As Knudsen number increases, rarefaction effects become more important and the continuum description of the gas begins to break down (the mean free path enlarges and momentum and energy transfer of collisions between molecules and surfaces become of the same significance as of inter-molecular collisions). However, although the moderate to strong rarefaction effects demand to model the flow following a particle-based approach like DSMC or a hybrid continuum-atomistic formulation, it seems that reasonably accurate results can be obtained in the early transition regime ($Kn < \sim 0.4$) with an extended hydrodynamics formulation or even with the NS description supplemented with a second-order $O(Kn^2)$ set of boundary conditions that also extend their applicability to higher Knudsen number, as it has been demonstrated in simple gas flows [9,11].
- $Kn > 10$: free-molecule regime ($\lambda \gg l$), the gas is considered highly rarefied and inter-molecular collisions are rare. The low rate of collisions implies that gas viscosity does not manifest itself and Reynolds number and, consequently, Eq. (1) is meaningless. In this regime, a solution of some form of the Boltzmann equation (i.e. the widely used particle-based technique DSMC) should be accomplished for a correct dealing of gas physics.

An estimation of the local rarefaction reached at the nozzle chamber and lip vicinity (outer zone) of the micronozzle at reference and operating conditions of interest in space applications is shown in Fig. 1 by means of a map of device size versus local pressure (geometrical dimensions corresponding to the three-dimensional flat micronozzle depicted in Fig. 2, whose data are specified in Table 1). The plot emphasizes that the gas behaves slightly rarefied through the throat and rarefaction progresses along the divergent portion of the nozzle, entering the early transitional regime in the outer portion of the divergent. The abrupt gas expansion at the lip vicinity implies the rapid rarefaction of the gas, going into the transition regime. According to the results of

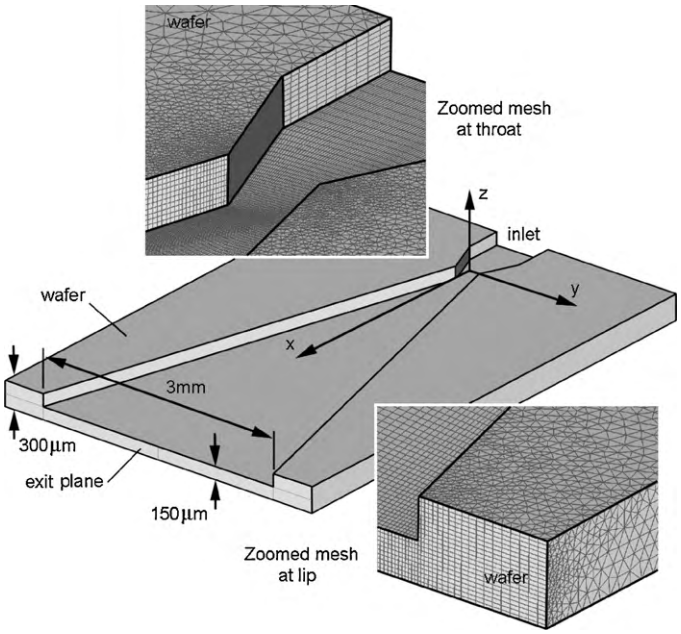

Fig. 2. Half-view of the microthruster geometry with the DeLaval 3D micronozzle. Flow region and wafer thickness are indicated.

previous work of the authors [8], the adopted modelling assumes that the gasflow is not far from local equilibrium, with Knudsen number varying across the micronozzle within the Knudsen range $0 \leq Kn \leq 0.4$.

Regarding the marginal limit $Kn \sim 0.4$, it is interesting to note that this Knudsen number can be formally interpreted as the ratio of the local thickness of the Knudsen layer to the nozzle local diameter (as the characteristic length) and in this case most of the nozzle cross-section would be filled by the rarefaction layer. Obviously, as the Knudsen layer fills a thicker portion of the cross-section, non-equilibrium effects become more and more dominant and the NS-based description reduces its applicability to a narrower zone by the nozzle centreline (the limiting case would correspond to about $Kn = 0.5$ with the Knudsen layer spanning the entire cross-sectional area). This interpretation helps to explain why the continuum-based approach supplemented with a second-order slip-model yields better results than first-order slip-models in flows of moderate Knudsen numbers and it seems an *a priori* appealing approach for the evaluation of overall performance of microdevices.

3. Numerical approach with solid–gas coupling

Steady-state simulations of a 3D micronozzle of rectangular cross-section operated with cold and hot gas discharging into very-low pressure quiescent ambient have been performed with the FLUENT code, solving the Navier–Stokes (NS) equations in the gas (N_2) coupled with the heat equation in the solid (silicon wafer) surrounding the fluid zone of the 3D computational domain. The schematic of the computational domain is depicted in Fig. 3a. It comprises the nozzle (solid material and gas regions) and a portion of the ambient where the nozzle discharges (near vacuum zone). The far-field vacuum boundary is placed two times the divergent length donwstream the nozzle exit. Nozzle symmetry planes permit to reduce the domain to 1/4 of its physical extension and the grid cell-size is chosen to assure grid-independence and adequate resolution of gradients using multiblock structured grid in the fluid region and unstructured in the solid (524,435 cells in total). The robust and effective second-order in Knudsen layer slip-flow conditions after Karniadakis and Beskok [12] has been implemented to

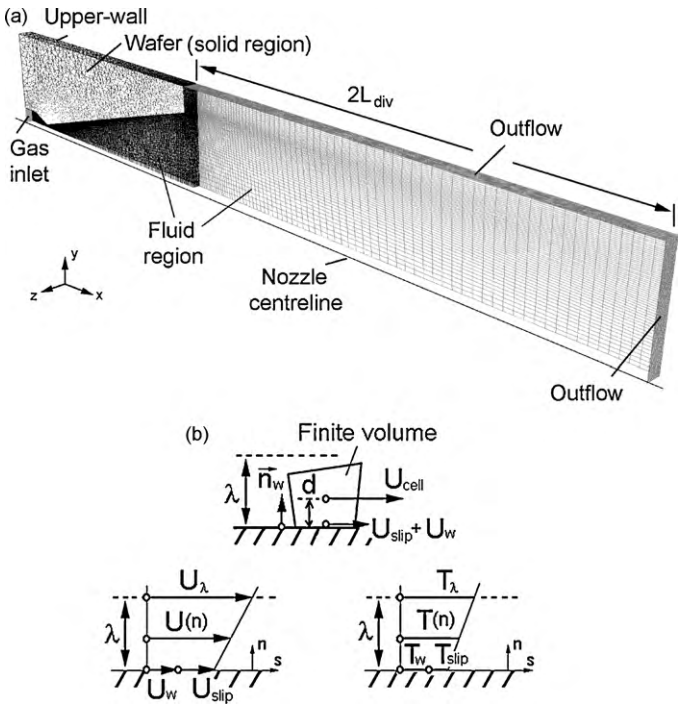

Fig. 3. (a) Layout of the 3D computational domain, that exploits the symmetry planes of the nozzle and (b) nomenclature of the finite-volume cell at the wall with slip-flow variables in the Knudsen layer of thickness $\sim\lambda$.

extend the range of applicability of the NS description beyond the Knudsen limit where the accuracy of the first-order slip law tends to fail. The flow evolves from near continuum in the gas supply chamber, passing through the slip-regime along the nozzle, to come under the early transition regime in the outer portion of the nozzle near the exit section. The intensification of non-equilibrium effects near the nozzle wall and mostly in the lip vicinity (where local rarefaction increases very quickly due to the gas expansion to the near vacuum media) suggests the marginal validity of the present NS-based description in this zone, that is confirmed by the reasonable agreement with DSMC solutions shown in the next section and in previous work [7].

The set of governing equations is discretized using a second-order upwind finite-volume formulation. Molecular nitrogen is assumed ideal and the flow is taken laminar (viscous dissipation damps the flow instabilities near the wall) with viscosity obeying the Sutherland's law. The model assumes negligible wall pressure gradients. The implementation of the second-order slip-flow model comprises the velocity slip (U_{slip}) at the nozzle wall according to the expression

$$U_{slip}-U_w=\frac{2-\sigma_v}{\sigma_v}\frac{lKn}{1-B(Kn)Kn}\left.\frac{\partial U_s}{\partial n}\right|_w+\frac{3}{4}\frac{\gamma-1}{\gamma}Pr\frac{k}{\partial R_g T_w}\left.\frac{\partial T}{\partial s}\right|_w \quad (2)$$

where the second term on the right hand is the thermal creep velocity (U_{creep}), U_w is the velocity of the wall, U_s is the tangential to wall velocity (tangent and normal vectors are indicated in Fig. 3b, $Pr=\mu C_p/k$ is the Prandtl number, Kn is the Knudsen number referred to the mean free path defined as $\lambda=\mu(\pi/2\rho p)^{1/2}$, and l is the lengthscale computed using the Gradient Length Local (GLL) formulae [11]

$$l=\min\left\{\frac{U_s}{|\nabla U_s\cdot\boldsymbol{s}|},\frac{T}{|\nabla T_s\cdot\boldsymbol{s}|},\frac{\rho}{|\nabla\rho\cdot\boldsymbol{s}|}\right\} \quad (3)$$

where T and ρ stand for static temperature and density, respectively. The GLL equation provides a preferred and robust procedure to build a lengthscale from local information in those flows that exhibit large variations of the properties in complex microgeometries, which is precisely the situation in supersonic flow. The term $B(Kn)$ is approximated by the first coefficient of its Taylor expansion $B(Kn)=b+cKn+O(Kn^2)$, as

$$B\approx b=\frac{l}{2}\left.\frac{d^2U_s/dn^2}{dU_s/dn}\right|_w \quad (4)$$

This substitution leads to a second-order condition. The temperature jump T_{slip} is proposed in analogy to U_{slip} from Smoluchowski [16]

$$T_{slip}-T_w=\frac{2-\sigma_T}{\sigma_T}\frac{2\gamma}{\gamma+1}\frac{l}{Pr}\frac{Kn}{1-B(Kn)Kn}\left.\frac{\partial T}{\partial n}\right|_w \quad (5)$$

where σ_v, σ_T are the accommodation coefficients for the momentum and energy, respectively, which depend on both the gas and the surface material properties. Thermal coupling at the solid–gas interface implies to enforce the temperature jump boundary condition and the heat-flux continuity across it at each iteration. Thus, making use of the notation of Fig. 3b, the heat flux balance at the gas (g) and solid (s) sides can be written

$$k_g\left.\frac{\partial T}{\partial n}\right|_w\approx k_g\frac{T_{slip}-T^g_{cell}}{d_g}=k_s\left.\frac{\partial T}{\partial n}\right|_w\approx k_s\frac{T^s_{cell}-T_w}{d_s} \quad (6)$$

with the wall surface temperature T_w computed in the course of the simulation. It is noted that heat-flux balance stated by Eq. (6) only comprises heat conduction since heat radiation is negligible in cold flow expansions. Its extension to handle more complex situations (e.g., supply or removal of energy at the wall due to external heating or active cooling) is not considered here. The implementation of the slip-flow model and heat-flux condition in FLUENT has been done with the User Defined Functions programming tool [13]. The discretized version of the slip-flow model reads

$$U_{slip}=\frac{U_{cell}\left(F_v/d+U_{creep}/U_{cell}\right)}{1+F_v/d} \quad (7)$$

$$T_{slip}=\frac{T_w+T_{cell}(F_v/d)}{1+F_T/d} \quad (8)$$

where

$$F_v=\frac{2-\sigma_v}{\sigma_v}\frac{lKn}{1-bKn},\qquad F_T=\frac{2-\sigma_T}{\sigma_T}\frac{2\gamma}{\gamma+1}\frac{l}{Pr}\frac{Kn}{1-bKn} \quad (9)$$

In 3D, the slip velocity vector $\mathbf{V}_{BC}$ imposed at the nozzle wall is built from the tangent projection of the nearest cell centre velocity vector, that is $\mathbf{V}_{BC}=U_{slip}\mathbf{V}_s/|\mathbf{V}_s|$, with $\mathbf{V}_s=\mathbf{V}_{cell}-(\mathbf{V}_{cell}\cdot\mathbf{n})\mathbf{n}$.

4. Results and discussion

4.1. Parametrical study

Since one of the largest potential source of uncertainty in microflows simulation is expected to be the modelling of the solid–gas surface interaction, a parametric study of its influence on the overall performance of the nozzle has been conducted by comparative simulation using a range of variation of the major parameters involved, thus to elucidate the sensitivity to these uncertainties. Specifically, the independent accommodation coefficients σ_v and σ_T of Eqs. (2) and (5), respectively, are adjustable parameters in the velocity slip and temperature jump expressions to estimate the momentum and energy losses on the gas–surface interface. That is, they account for the collisions of the gas molecules with the wall and feature the incomplete accommodation in the process of momentum and thermal energy transfer between incident molecules and the solid boundary.

Table 2
Reference and operating flow conditions.

Agent gas: molecular nitrogen (N_2)		
Specific heat ratio	$\gamma = C_p/C_v$	1.4
Near vacuum static pressure	p_∞	10 Pa
Reference chamber conditions		
Stagnation pressure	$p_{t,o}$	10,000 Pa
Stagnation temperature	$T_{t,o}$	300 K
Operating chamber conditions		
Stagnation pressure	$p_{t,o}$	50,000 Pa
Stagnation temperature	$T_{t,o}$	2000 K (hot) 300 K (cold)

Extensive literature exists dealing with the complicated measurements and experimental uncertainties of momentum and thermal accommodation coefficients for different combinations of solids with monatomic and diatomic gases [14,15], that stresses the complex dependence, sensitivity and wide variation of these coefficients with the gas and surface temperature and physical characteristics (molecular weight, roughness, . . .) for several combinations of interest and which remains an open topic of research. For nitrogen in contact with most engineering surfaces, particularly silicon, experimentally derived σ_T ranges from 0.87 to 1. In the case of σ_v an appreciably wider range of variation is expected, with values down to 0.7 found for the pair N_2–Si according to microchannel experiments.

The present study addresses the effect of varying σ_v over the interval [0.4, 1] with σ_T taken unity for simplicity. The full thermal accommodation assumed in the present study favours the thermal exchange rate between gas and solid as it implies that temperature of colliding N_2 molecules adapts itself to the silicon surface temperature.

The steady-state simulations performed in this study for the 3D-Flat micronozzle can be grouped into two subsets: sensitivity study and performance simulations according to the nozzle working conditions specified in Table 2. The first group of simulations comprises the sensitivity analysis conducted for the termed reference chamber conditions, characterized by a relatively low stagnation pressure at the nozzle inlet. In addition, these reference conditions permit the comparison with the DSMC solution of Alexeenko et al. [3,4] for this 3D-Flat nozzle at identical operating conditions, with wall temperature $T_w = 300$ K and diffuse reflection coefficient $\sigma_v = 1.0$ to model the surface–molecule interaction. The sensitivity study comprises the following sets of test cases:

Varying the thermal boundary condition at the upper-wall of the wafer (see Fig. 3a) for $\sigma_v = 0.8$, $\sigma_T = 1.0$. The simulations comprise the baseline case defined by prescribing thermal insulation BC (adiabatic) at the upper-wall; and three simulations corresponding to an isothermal BCs set at the upper-wall: $T_w = 100$ K, 200 K and 300 K.
Varying the momentum accommodation coefficient σ_v, for $\sigma_T = 1.0$ and adiabatic BC at the upper-wall. The cases considered are $\sigma_v = 0.4$, 0.6, 0.8 and 1.0.
Varying the momentum accommodation coefficient σ_v, for $\sigma_T = 1.0$ and isothermal BC $T_w = 300$ K at the upper-wall. The values considered are $\sigma_v = 0.4$, 0.6, 0.8 and 1.0.

The simulation computed with isothermal BC $T_w = 300$ K at the upper-wall and $\sigma_v = 1.0$ is the best suited for comparison purposes with the DSMC results. It is noted that the high thermal conductivity of silicon ($k_{Si} = 149$ W/mK) leads to a highly uniform temperature field in the wafer substrate. Therefore, prescribing T_w at the upper-wall results in a rather fine control of the temperature at the solid side of the gas–solid interface (it performs as an effective imposition of the upper-wall BC onto the solid–gas interface).

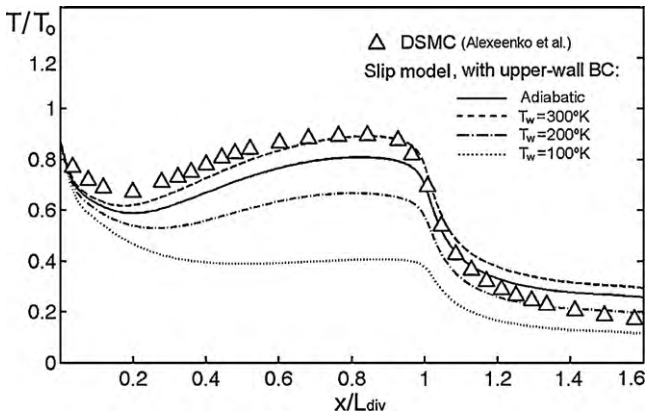

Fig. 4. Normalized temperature along the axis of the nozzle, corresponding to four different BCs set at the upper-wall of the Si-wafer, for validation flow conditions. DSMC data from [4].

The second group comprises two simulations carried out with cold and hot gas entering the nozzle at stagnation pressure $p_c = 50{,}000$ Pa (adiabatic upper-wall BC and $\sigma_v = 0.8$, $\sigma_T = 1.0$ are considered), such that it mimics a more realistic working situation of micronozzles intended for space propulsion.

4.2. Sensitivity to the solid–gas interface BC

Figs. 4 and 5 show the normalized static temperature and axial velocity, respectively, along the nozzle centreline computed for $\sigma_v = 0.8$ and various temperature conditions set at the upper-wall of the wafer. The comparison clearly reveals the strong dependence of the gas expansion with the thermal boundary conditions imposed at the wafer surface. In particular, the maximum variation experienced by the bulk region inside the nozzle between simulations results to be of about 150 K in temperature and 40% of velocity magnitude. This clearly shows that the correct specification of temperature at the solid side of the solid–gas interface is crucial for an accurate prediction of the nozzle performance. However, it is not possible to prescribe its value *a priori* at the solid–gas interface although the temperature is almost uniform in the solid region

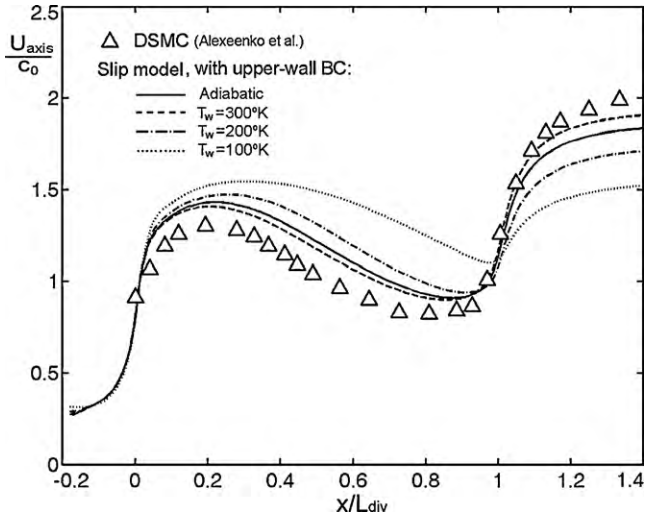

Fig. 5. Normalized velocity with the chamber sound speed (c_0) along the axis of the nozzle, corresponding to four different BCs set at the upper-wall of the silicon wafer, for validation flow conditions. DSMC data from [4].

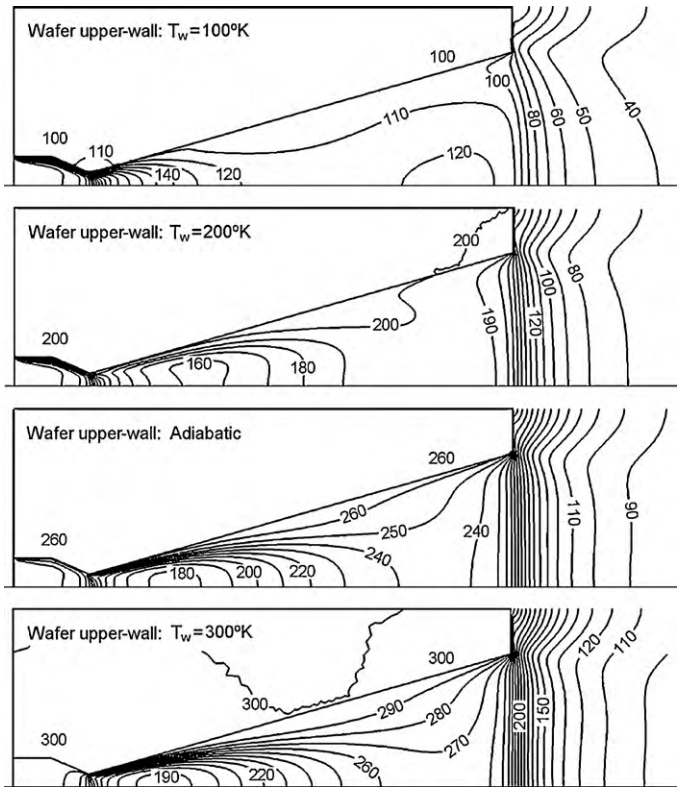

Fig. 6. Steady-state temperature map at the *xy*-centreplane of the nozzle for p_c = 10,000 Pa, computed with four different energy-BC set at the external-wall of the silicon wafer. From top to bottom: isothermal-wall T_w = 100 K; isothermal-wall T_w = 200 K; isolated-wall (adiabaticity); and isothermal-wall T_w = 300 K.

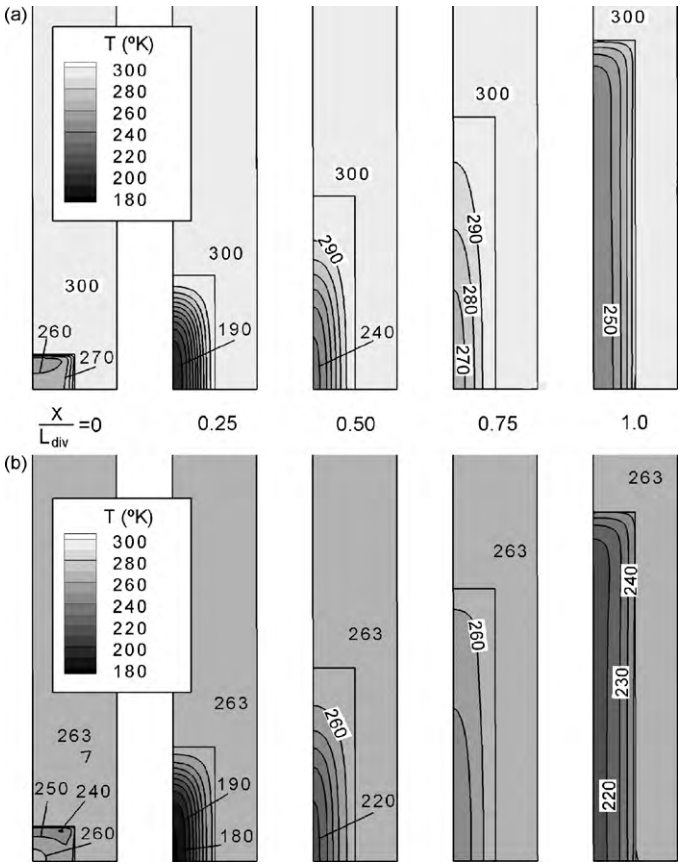

Fig. 7. Steady-state temperature iso-contours at nozzle cross-sections x/L_{div} = 0, 0.25, 0.5, 0.75 & 1, computed for COLD-Flow at p_c = 10,000 Pa: (a) isothermal nozzle T_w = 300 K set at the external wall of the silicon wafer (b) adiabatic nozzle: isolated-wall BC set at the external wall.

as it is seen in the temperature maps of Fig. 6. Its determination demands to solve the heat equation in the solid region coupled with the NS equations in the gas region, thus solid surface temperature turns to be a result of the simulation.

Besides the higher sensitivity of the bulk gas temperature to the thermal BC compared with the velocity profiles, it is worth noting that the temperature drop occurring downstream the throat section is followed by a somehow flatten profile in the outer part of the divergent. The examination of this fairly flat value of temperature reveals that it is rather close to the wafer temperature in the four cases analysed, which reveals the tendency to reach uniform temperature (gas thermalization) in the outer part of the divergent. This behaviour is mainly attributed to the side-walls of the nozzle, that act in two ways: first and opposite to the role of the expansion-walls (flap-walls) which drive the expansion, the side-walls confine the gas without contributing to augment the nozzle cross-sectional area. Contrary to the relatively thin boundary layers that develop near the throat, the progressive thickening rate of the boundary layers on the walls, mainly over the side-walls in the outer portion of the nozzle, provokes the flow blockage and deceleration due to viscosity, thus making the gas expansion ineffective. And second, side-walls participate with the largest contribution to the ratio of surface area-to-volume, thus heat transfer is enhanced in this region up to the nozzle lip (in addition, σ_T = 1 implies the minimization of the thermal energy loss, so thermalization is favoured). However, it is interesting to note that gas thermalization is incomplete as it is seen in the temperature maps plotted at the *xy*-centreplane of the nozzle in Fig. 6: a temperature range of about 150 K is observed to occur in the bulk flow in the outer region of the nozzle when T_w changes from 100 K to 300 K. Simulations show that a temperature shift of about 20–30 K between the centreline and the wall persists. The rapid cooling experienced by the gas near the exit section is visible out of the accumulation of isotherms, as well as the strong gas acceleration that follows in this zone is a consequence of its adaptation in pressure to the ambient. The pattern of isotherms close to the lip evidences the local flow turn and three-dimensional character of the flowfield in this region. The details of the temperature field along the nozzle can be inspected from the five cross-sections equally spaced from the throat (x/L_{div} = 0) to the exit (x/L_{div} = 1) depicted in Fig. 7 for the simulations performed with isothermal-wall T_w = 300 K and insulated-wall BC. In particular, the simulation with the insulated-wall BC exhibits a steady-state temperature in the wafer of about 263 K. This temperature value in the wafer, under 300 K, indicates that the flow expansion behaves efficiently in extracting heat from the surrounding solid material. In the simulation conducted with the isothermal-wall T_w = 300 K BC, the surrounding material acts as a thermal source: heat is released from the solid to the gas, making the average temperature of the gas to increase over the values found in the simulation with insulated-wall. A closer examination of the temperature field in the outer portion of the divergent (cross-sections x/L_{div} = 0.75 and exit section) permits to quantify the temperature increase of about 30 K with regard to the adiabatic case, which is linked to the rather large contact surface with the wafer in this region. The different participation of the flap and side walls in the gas expansion and thermal balance near the throat and in the outer portion of the nozzle is visible out of the temperature maps at corresponding cross-sections for both simulations. Hence, at the throat vicinity an asymmetric temperature profile develops with a bulge located under the flap-wall caused by the local acceleration of the flow. At downstream sections, the temperature continues to drop in the flow core driven

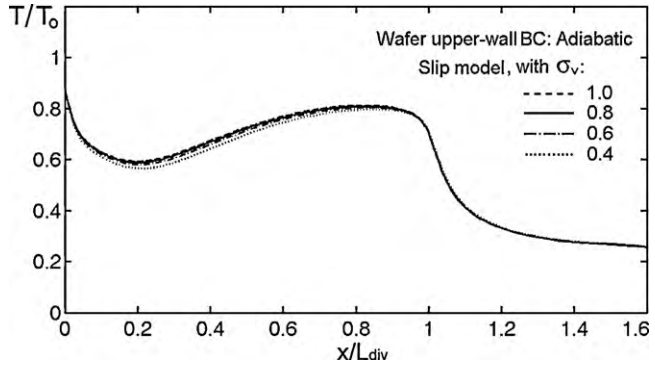

Fig. 8. Normalized temperature along the axis of the nozzle, corresponding to adiabatic upper-wall BC and accommodation coefficient σ_v = 0.4, 0.6, 0.8, 1.0.

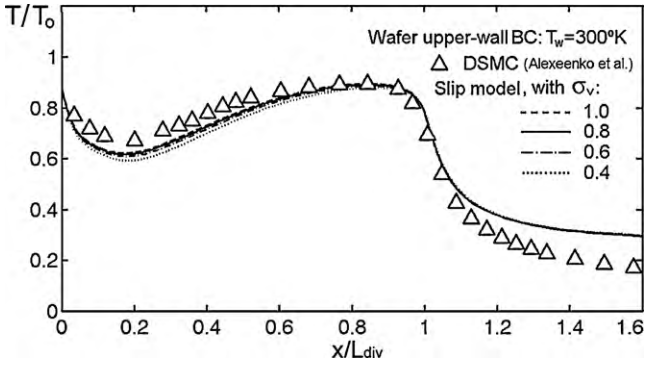

Fig. 10. Normalized temperature along the axis of the nozzle, corresponding to isothermal upper-wall BC and accommodation coefficient σ_v = 0.4, 0.6, 0.8, 1.0. DSMC data from [4].

by the area expansion but the viscous effects make this mechanism ineffective and flow thermalization imparted by the walls begins to dominate, which is precisely the situation already discerned at x/L_{div} = 0.75. The strong temperature gradients normal to the wall and rapid departure from thermalization at the exit section is a consequence of the abrupt radial expansion experienced by the gas as it exits the nozzle.

The comparison of the DSMC solution with the NS results for the isothermal-wall T_w = 300 K exhibits an overall good agreement up to the exit section of the nozzle, with a progressive departure of solutions outside the nozzle due to rarefaction. The moderate discrepancy visible inside the nozzle is mainly attributed to the different computational domain extension and cell-size used in both simulation approaches, motivated by the solvers constrains in each case. Besides, it should be noticed that the inclusion of a wafer zone in the continuum-based simulation (not present in the DSMC simulation) must necessarily have a minimal influence onto the solution deviation observed to occur in the outer zone of the divergent portion, since a very uniform temperature, close to 300 K, is attained in the solid side of the solid–gas interface of the case compared.

The results of the performance sensitivity to the momentum accommodation coefficient shown for the insulated-wall case in Figs. 8 and 9 and for isothermal-wall T_w = 300 K in Figs. 10 and 11, reveal a small to moderate dependence of the bulk flow velocity and temperature profile, with a maximum variation of about 2–4% when σ_v goes from 0.4 to 1.0. The decrease of maximum bulk velocity with σ_v has its origin in the conservation of massflow rate through the nozzle. It is known that flow slip implies a smaller normal gradient of the velocity $\partial u/\partial n$ at the wall, then a lower friction stress and fuller velocity profiles near the wall occur as σ_v gets higher. Since rarefaction effects at the throat vicinity are still very small, the tiny velocity slip at this section leads to quite similar massflow rates passing through the nozzle for a given thermal boundary condition set at the wafer upper-wall. Consequently, as the velocity profile gets fuller by the wall, the magnitude of the bulk velocity at the axis decreases to satisfy the mass conservation.

The comparison of the temperature profiles computed with the slip-flow model for the isothermal T_w = 300 K BC (Figs. 10 and 11) reveals that a less percentual sensitivity of the static temperature with σ_v exists, which is a consequence of the flow thermalization. This behaviour is visible in the corresponding meridian maps provided in Fig. 6, where the temperature gradient established between the nozzle wall and centreline is only slightly affected by the variation of σ_v in comparison with the velocity case.

The prediction provided by the slip-flow model can be evaluated from its comparison with the DSMC solution, plotted superimposed in the above-mentioned figures for the isothermal-wall T_w = 300 K. The comparison states the good agreement attained, however a slight deviation of the velocity slip inside the divergent portion of the nozzle is suggested by the plots. It seems that a more efficient expansion is obtained in the continuum-based calculation as it is

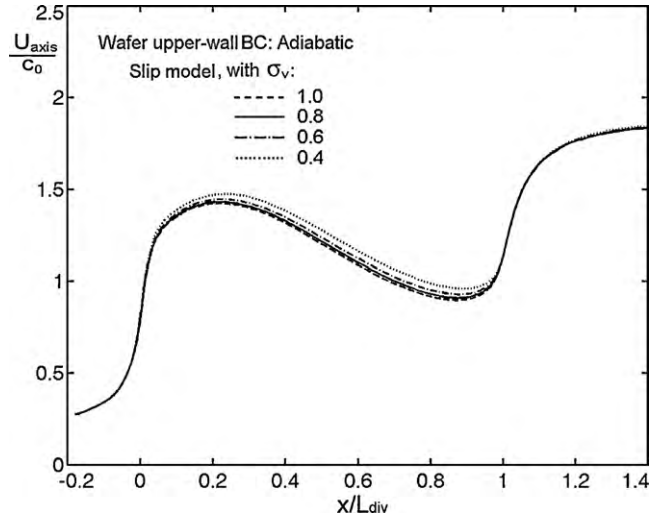

Fig. 9. Normalized velocity with the chamber sound speed (c_0) along the axis of the nozzle, corresponding to adiabatic upper-wall BC and accommodation coefficient σ_v = 0.4, 0.6, 0.8, 1.0.

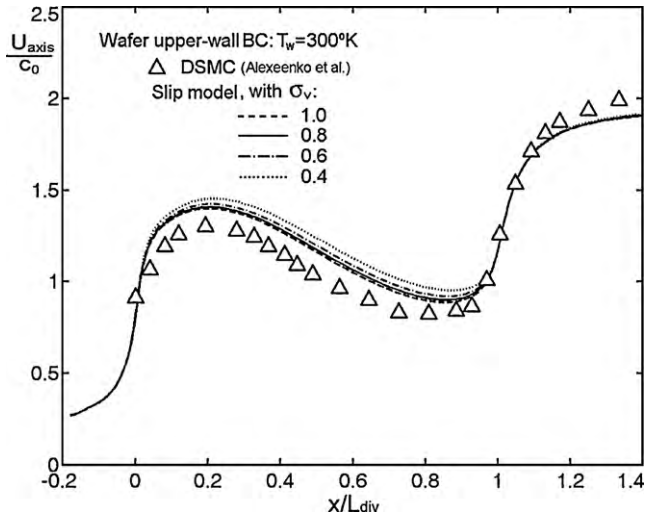

Fig. 11. Normalized velocity along the axis of the nozzle, corresponding to isothermal upper-wall BC and accommodation coefficient σ_v = 0.4, 0.6, 0.8, 1.0. DSMC data from [4].

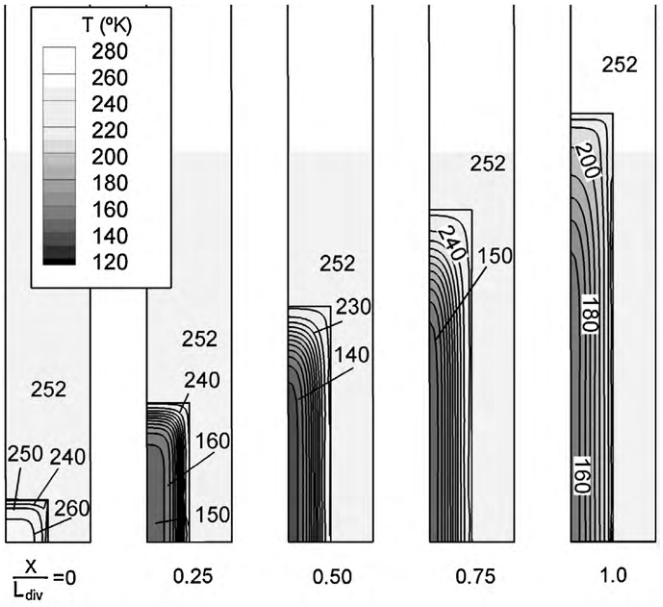

Fig. 12. Steady-state temperature iso-contours at cross-sections x/L_{div} = 0, 0.25, 0.5, 0.75 & 1 of the nozzle modelled adiabatic, computed for COLD-Flow at p_c = 50,000 Pa.

inferred from the relative location of the bulk velocity and temperature curves over the DSMC points for all the σ_v range considered.

4.3. Performance at operating flow conditions

The chamber pressure p_c = 10,000 Pa of the preceding subsection used for comparison with available DSMC results, turns out to be a rather low pressure level. In fact, realistic operation in space propulsion is foreseen to demand much higher pressure level, in the order of one to tens of bars, to achieve reasonable nozzle performance. Consequently, higher characteristic velocities will be expected in micronozzles flows and viscous dissipation will play a major role on converting kinetic energy into heat and coupling velocity and thermal fields.

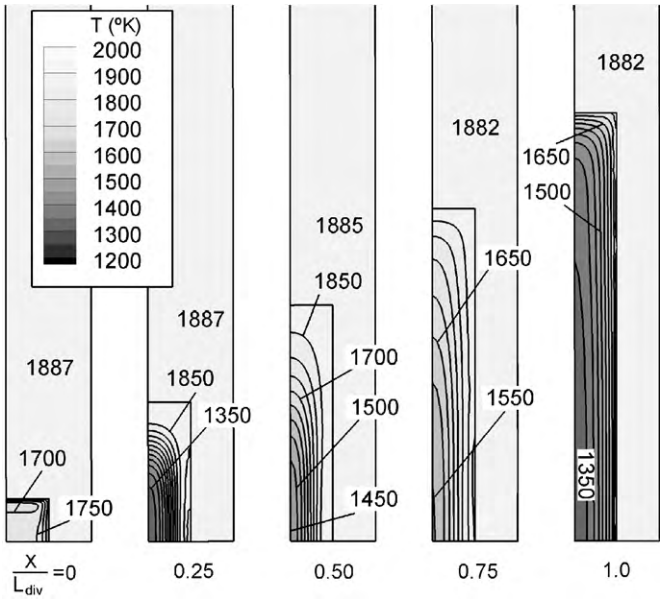

Fig. 13. Steady-state temperature iso-contours at cross-sections x/L_{div} = 0, 0.25, 0.5, 0.75 & 1 of the nozzle modelled adiabatic, computed for HOT-Flow at p_c = 50,000 Pa.

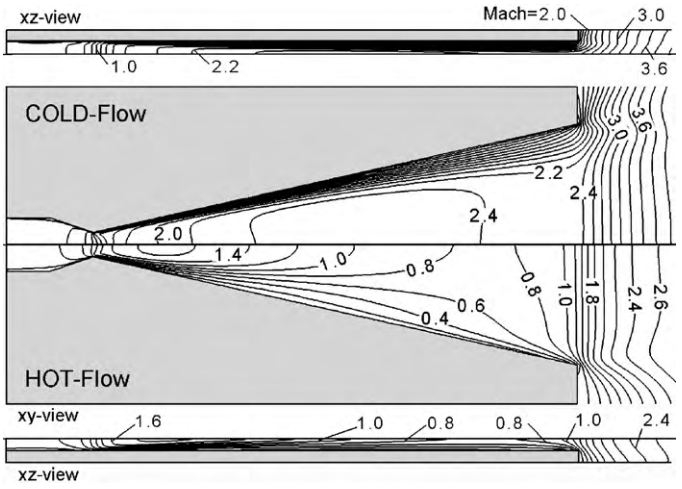

Fig. 14. Steady-state Mach iso-contours at nozzle centerplanes computed for the COLD- and HOT-Flow simulation at p_c = 50,000 Pa.

In this subsection some results of computations carried out at p_c = 50,000 Pa with COLD- and HOT-flow are presented and their differences discussed. These differences are notorious due to the profound impact of the supply gas temperature in the viscous effects, as the Reynolds number anticipates (Re ≈ 2140 in COLD-flow and Re ≈ 233 in HOT-flow, referred to the throat conditions). Hence, a much thicker boundary layer in relation to the nozzle deep develops in HOT-flow, that is already visible at x/L_{div} = 0.25 from the comparison in Figs. 12–14. Besides, while a somehow inviscid core can be discerned in the COLD-flow field up to the half-length of the divergent part, this region quickly disappears in the HOT-flow

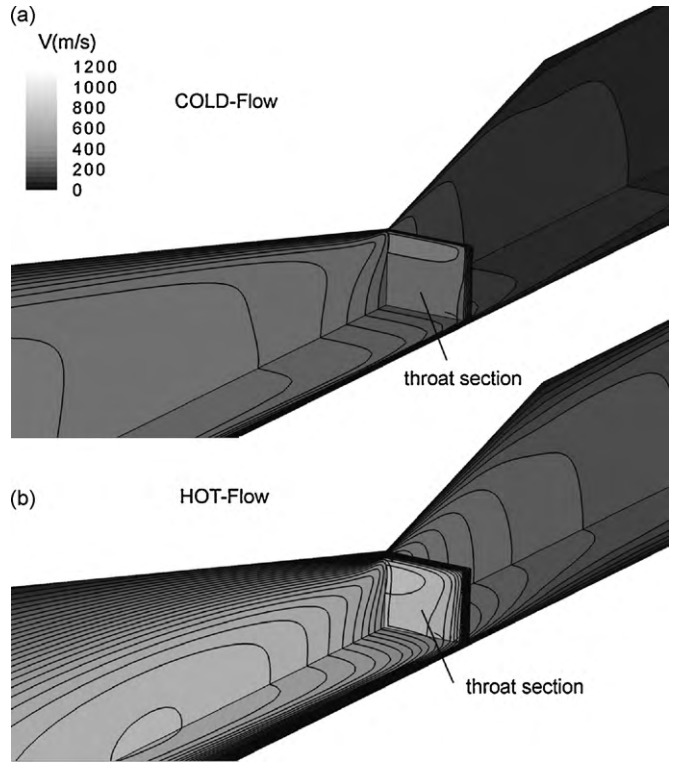

Fig. 15. Steady-state velocity iso-contours at centreplanes and throat cross-section of the nozzle, computed at p_c = 50,000 Pa for: (a) COLD-Flow and (b) HOT-Flow simulation.

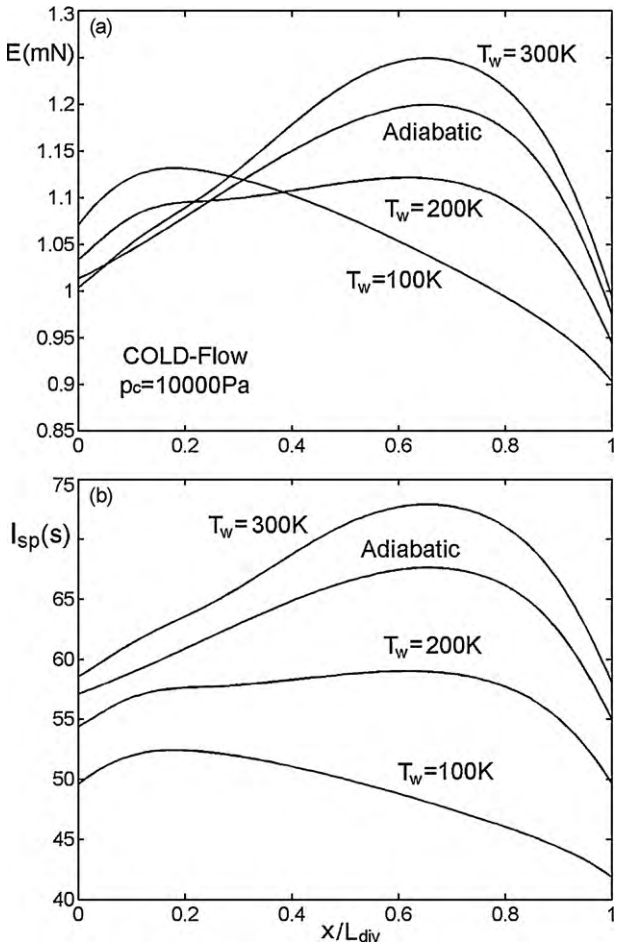

Fig. 16. Nozzle performance with COLD-Flow at p_c = 10,000 Pa: (a) thrust and (b) specific impulse versus normalized axial length (accommodation coefficients correspond to σ_v = 0.8, σ_T = 1.0).

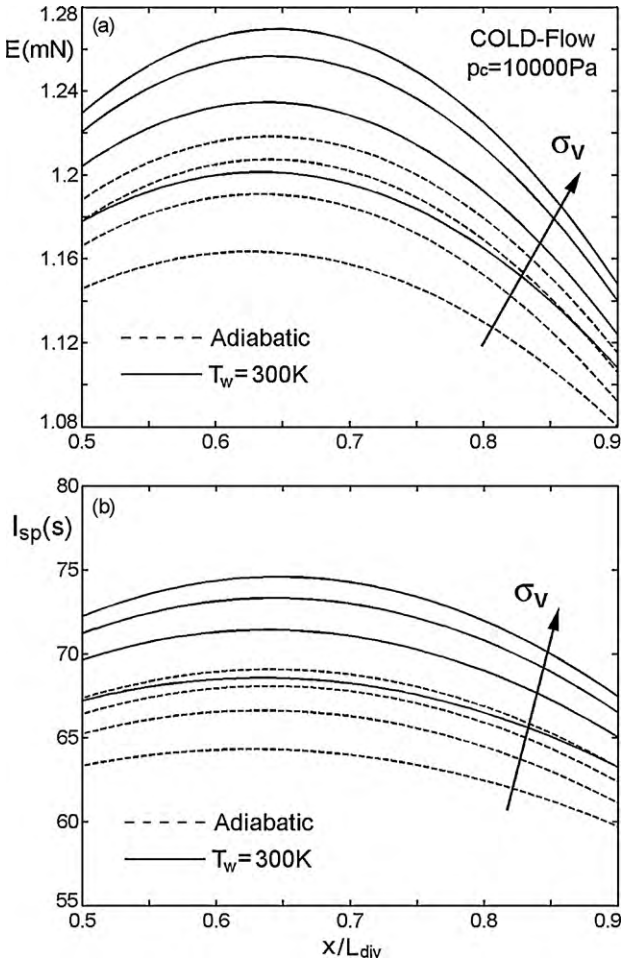

Fig. 17. Nozzle performance with COLD-Flow at p_c = 10000 Pa for σ_v = 0.4, 0.6, 0.8 & 1.0, computed with adiabatic and isothermal T_w = 300 K upper-wall: (a) thrust and (b) specific impulse versus normalized axial length.

case because the boundary layers occupy the entire cross-section just after the first third of the nozzle length, as it is visible in the temperature maps of Fig. 13 (the dense accumulation of isotherms along the side-walls seen for x/L_{div} = 0.75 in COLD- and x/L_{div} = 0.5 in HOT-flow indicates the complete penetration of the thermal layer). It is noted that higher supply stagnation pressure implies higher characteristic velocities of the gas, then a lower wafer steady-state temperature in the COLD-flow simulation is achieved, as expected (252 K instead of 263 K for p_c = 10,000 Pa). Temperature maps at cross-sections in Fig. 13 for HOT-flow simulation permit to quantify the small spatial variation of the wafer temperature within 0.2% (1887 K at the throat versus 1882 K at exit), so uniform temperature is attained into the solid. The much higher rate of boundary layer growth with HOT-flow is evident out of the iso-Mach field plotted in Fig. 14 and velocity maps of Fig. 15. In addition, the rapid growing rate of the boundary layer along the flap and side-wall is discerned from the corresponding iso-Mach field given at the *xy*- and *xz*-centreplanes, respectively. In fact, this rapid thickening of the viscous layer on the side-walls drives the flow blockage and hinders the gas expansion, which occurs earlier in the HOT-flow case. A close inspection of the HOT-flow field reveals that the gas undergoes an early shockless deceleration from supersonic to subsonic within the midway region of the divergent. A similar phenomenon is detected for COLD-flow but, in this case, the higher Reynolds number makes the full blockage to shift toward the end portion of the nozzle, thus shockless deceleration to subsonic is delayed. The rapid acceleration to supersonic (and reduction of the gas temperature) that follows near the exit section seen in Fig. 14 and also visible out of the velocity profiles plotted in Figs. 5, 9 and 11, has its origin in the final gas discharge into the near vacuum media. It is precisely the setup of the insulated-wall BC in both simulations what clarifies that the observed shockless deceleration is the consequence of the viscous dissipation and not a phenomenon driven by the net thermal-flux across the solid–gas interface. Hence, viscous dissipation acts converting mechanical energy of the flow into heat, so the combined effect of lowering the flow velocity and increasing the static temperature leads to a Mach deceleration inside the nozzle. A more detailed investigation of the role of viscous dissipation has been provided by the authors in [7,8] for an axisymmetrical micronozzle, whose much higher expansion ratio implies higher gas velocities and, as a result, the action of the viscous stresses becomes dominant in the flowfield solution.

The main parameters for performance assessment are the thrust force *E*, determined by

$$E = \int_A (\rho U^2 + p - p_\infty)\ \mathrm{d}A \tag{10}$$

where *U*, *p* and *A* are the local axial velocity, static pressure and cross-sectional area of the nozzle, respectively); and the specific impulse I_{sp}, defined as thrust per weight flow (that is, E/gG_{th}, being G_{th} the massflow rate). Hence, it is interesting to plot their variation as a function of the length of the nozzle for the values of

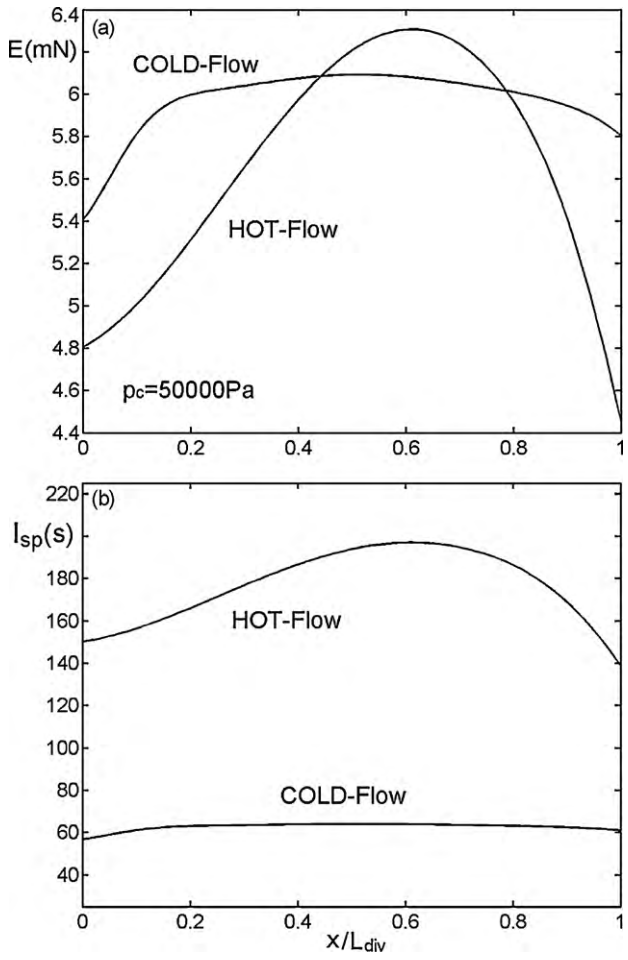

Fig. 18. Delivered nozzle performance with COLD- and HOT-Flow at p_c = 50,000 Pa: (a) thrust and (b) specific impulse versus normalized axial length (accommodation coefficients correspond to σ_v = 0.8, σ_T = 1.0).

slip-flow model coefficients and wafer thermal-BC considered in the present study. Figs. 16 and 17 provide the results corresponding to COLD-Flow at p_c = 10,000 Pa with σ_v = 0.8 in the slip-flow model. Essentially, thrust and specific impulse change rapidly in the end portion of the nozzle and the presence of a maximum at an intermediate cross-section is clearly discerned in all cases. Whereas in the simulation performed with an adiabatic-wall this pronounced drop is mainly attributed to the viscous stresses at the solid–gas surface and bulk flow, in the isothermal-wall cases the viscous stresses action is superimposed with the heat exchange at the solid–gas interface. This heat flux across the wall may be beneficial, as it happens for T_w = 300 K, where the wafer releases heat to the gas, so a net gain of performance takes place. However, when the wafer temperature is too low, it may act degrading the generation of thrust and I_{sp} as there exists a thermal loss from the gas (which is the situation for T_w = 100 K: the wafer removes heat from the gas and provokes its intense cooling just downstream the throat).

Performance for varying σ_v is given in Fig. 17, corresponding to the COLD-flow simulation at p_c = 10,000 Pa with isothermal (T_w = 300 K) and adiabatic boundary condition set at the wafer upper-wall. Higher sensitivity is observed in the isothermal BC simulation from direct inspection and, specifically, the maximum change in thrust and I_{sp} within the range of σ_v variation corresponds to $\Delta E \sim 5.5\%$ and $\Delta I_{sp} \sim 8.5\%$ for the isothermal wafer; and $\Delta E \sim 4.7\%$ and $\Delta I_{sp} \sim 7.3\%$ in the adiabatic case.

The form of the curves clearly states that nozzle performance depends to a large extent on the thermal BC prescribed onto the wafer surface, as well as moderately on the slip-flow factor σ_v. Furthermore it is inferred the convenience of providing a shorter divergent portion, up to the section of maximum thrust, and those material surfaces with the highest σ_v to minimize losses and achieve E and I_{sp} optimization.

At operating pressure p_c = 50,000 Pa similar behaviour is found (see Fig. 18), but now the thrust plot exhibits a higher maximum (over 6 mN) because of the higher supply pressure, as expected. Interestingly, for COLD-flow conditions the variation of thrust with the axial location shows a rather flat profile in contrast with the more abrupt variation in HOT-flow. Thus, the comparison reveal that COLD-flow provides a more insensitive performance to the nozzle length, which constitutes an attractive feature from the performance predictability standpoint.

5. Conclusions

A methodology to simulate high-speed gasflow in micronozzles supplementing the Navier–Stokes equations with a second-order slip-flow model and including thermal coupling at the solid–gas interface is presented to elucidate the sensitivity of the nozzle performance to the solid–gas interaction. For this task, COLD- and HOT-flow simulations with low and moderate operational supply gas pressure conditions have been considered in the investigation. The nozzle chamber conditions of low pressure have also served as an assessment testcase for the slip-flow model and it has demonstrated the overall agreement with the DSMC data, albeit the comparison reveals that the Navier–Stokes based approach imparts a small mismatch of the slip at the wall. Quantification of the thrust force and specific impulse dependence with the momentum accommodation coefficient shows a moderate variation of about 6% and 9%, respectively. Additionally, the strong influence of the wafer thermal boundary condition on the flow field and, as result, on the nozzle performance, is accentuated by the low aspect-ratio of the nozzle considered and large surface effects at small Reynolds number. Essentially, it is concluded that friction and heat transfer over the side-walls must be correctly accounted for to characterize MEMS-class nozzles.

Acknowledgements

This research was funded by the Spanish Ministry of Defence as part of the micropropulsion activities in the Small Satellites Programme of the Instituto Nacional de Técnica Aeroespacial. We wish to thank Ruth Lobo del Olmo of INTA for her kind support with the computing facilities.

References

[1] W. Grout, S. Olson, Chemical Microthruster Options, CR-198531, NASA, 1996.
[2] A. Alexeenko, D.A. Fedosov, S.F. Gimelshein, D.A. Levin, R.J. Collins, Transient heat transfer and gas flow in a MEMS-based thruster, J. Microelectromech. Syst. 15 (1) (2006) 181–194.
[3] A. Alexeenko, D.A. Levin, D.A. Fedosov, S.F. Gimelshein, R.J. Collins, Performance analysis of microthrusters based on coupled thermal-fluid modelling simulation, J. Propul. Power 21 (1) (2005) 95–101.
[4] A. Alexeenko, D.A. Levin, S.F. Gimelsheim, R.J. Collins, B.D. Reed, Numerical modelling of axisymmetric and three-dimensional flows in microelectromechanical systems nozzles, AAIA J. 40 (5) (2002) 897–904.
[5] A.D. Ketsdever, D.C. Wadsworth, E.P. Muntz, Gas–surface interaction model influence on predicted performance of microelectromechanical system resistojet, J. Thermophys. Heat Transfer 15 (3) (2001) 302–307.
[6] Z.X. Sun, Z.Y. Li, Y.L. He, W.Q. Tao, Coupled solid (FVM)-fluid (DSMC) simulation of micro-nozzle with unstructured-grid, J. Microfluid Nanofluid (2009), doi:10.1007/s10404-009-0418-5.
[7] J.A. Moríñigo, J. Hermida-Quesada, Analysis of viscous heating in a micro-rocket flow and performance, J. Therm. Sci. 17 (2) (2008) 116–124.

[8] J.A. Moríñigo, J. Hermida-Quesada, Simulation of high-speed flow in μ-rockets for space propulsion applications, in: Proc IUTAM Symposium on Advances in Micro- and Nanofluidics, 2007, pp. 175–189.
[9] S. Colin, Rarefaction compresibility effects on steady and transient gas flows in microchannels, J. Microfluid Nanofluid 1 (2005) 268–279.
[10] J. Maurer, P. Tabelling, P. Joseph, H. Willaime, Second-order slip laws in microchannels for helium and nitrogen, Phys. Fluids 15 (9) (2003) 2613–2621.
[11] N.G. Hadjiconstantinou, Validation of a second-order slip model for dilute gas flows, Microscale Thermophys. Eng. 9 (2) (2005) 137–153.
[12] G. Karniadakis, A. Beskok, Micro-Flows: Fundamentals and Simulation, Springer Verlag, Heidelberg, 2002.
[13] Fluent Inc., Fluent 6.3 UDF Manual, Fluent Inc., Lebanon, 2006.
[14] E.B. Arkilic, K.S. Breuer, M.A. Schmidt, Mass flow tangential momentum accommodation in silicon micromachined channels, J. Fluid Mech. 437 (2001) 29–43.
[15] D.J. Rader, M.T. Wayne, J.R. Trott, J.R. Torczynski, J.N. Castañeda, T.W. Grasser, Measurements of Thermal Accommodation Coefficients, Sandia National Laboratories Report, SAND2005-6084, October, 2005.
[16] M. Smoluchowski, Über den Temperatursprung bei Wärmeleitung in Gasen, Akad. Wiss. Wien. 107 (1898) 304–329.

Biographies

José Antonio Moríñigo was born in 1970. He graduated in Aeronautical Engineering from the Polytechnic University of Madrid, Spain, in 1995 and obtained his PhD degree in engineering in 2003 from the same university. He joined the National Institute for Aerospace Technology (INTA, Madrid) in 1998 where he is currently involved in space programmes, with the main topic covering engineering and applied research of chemical propulsion systems for very small spacecrafts and space applications.

José Hermida-Quesada was born in 1964. He received his master degree in Aeronautical Engineering from the Polytechnic University of Madrid, Spain, in 1990. Currently he is a researcher in the National Institute for Aerospace Technology (INTA, Madrid). His fields focus the development and testing of solid and hybrid rocket motors both for space and tactical applications.